Engineering Geology 335 (2024) 107538

Contents lists available at ScienceDirect

Engineering Geology

journal homepage: www.elsevier.com/locate/enggeo

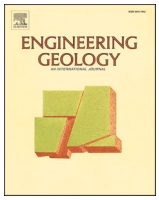

Hydromechanical modeling of evolving post-wildfire regional-scale landslide susceptibility

Masood Abdollahi [a], Farshid Vahedifard [b,c,*], Ben A. Leshchinsky [d]

[a] Terracon Consultants Inc., Mountlake Terrace, WA 98043, USA
[b] Department of Civil and Environmental Engineering, Tufts University, Medford, MA 02155, USA
[c] United Nations University Institute for Water, Environment and Health (UNU-INWEH), Richmond Hill, ON L4B 3P4, Canada
[d] Department of Forest Engineering, Resources and Management, Oregon State University, Corvallis, OR 97331, USA

ARTICLE INFO

Keywords:
Wildfire
Landslide susceptibility mapping
Physics-based model
Unsaturated soil
Rainfall
GIS

ABSTRACT

Post-wildfire mass wasting is a major problem throughout many regions worldwide. Recent dramatic increases in global wildfire activities coupled with a shift in wildfire-prone elevation to higher altitudes raise the need to better predict post-fire rainfall-triggered landslides. Despite its importance, only a limited number of studies have investigated landslide susceptibility in areas hit by wildfires using hydromechanical models. However, most of these studies follow either qualitative or semi-quantitative approaches without explicitly considering the fire's effects on the impacted area's physical behavior. This study aims to develop and employ a physics-based framework to generate susceptibility maps of rainfall-triggered shallow landslides in areas disturbed by wildfire. A coupled hydromechanical model considering unsaturated flow and root reinforcement is integrated into an infinite slope stability model to simulate the triggering of shallow landslides from rainfall. The impact of fire is considered through its effects on soil and land cover properties, near-surface processes, and canopy interception. The developed model is then integrated into a geographic information system (GIS) to characterize the regional distribution of landslide potential and its variability considering topography, geology, land cover, and burn severity. The proposed framework was tested for a study site in Southern California. The site was burned in the San Gabriel Complex Fire in June 2016 and experienced widespread landsliding almost three years later following an extreme rainstorm in January 2019. The proposed framework could successfully model the location of observed shallow landslides. The model also revealed a significantly higher likelihood for slope failure in areas burned at moderate to high severities as opposed to unburned and low-burn severity areas. The findings of this study can be employed to predict the timing and general locations of rainfall-triggered shallow landslides following wildfires.

1. Introduction

Recent increases in wildfire activities and shifts in their frequency, intensity, and seasonality have raised major concerns about socioeconomic and environmental impacts stemming from cascading hazards around the world. The changes in fire regime are mainly attributed to climate and land-use changes as well as warming temperatures, prolonged drought, reduced snowpack, decreases in warm season precipitation frequency, and fire suppression over the last century (Abatzoglou and Williams, 2016; Burke et al., 2021; Madadgar et al., 2020; Williams et al., 2019). Since the 1980s, the annual area burned in wildfires has increased fivefold in the United States, punctuated by massive wildfires in 2018 and 2020 (NIFC, 2022). The wildfire-induced changes to affected areas may leave them susceptible to a variety of post-fire geohazards, such as debris flows, landslides, and soil erosion long after burning (Moody et al., 2013; Shakesby and Doerr, 2006; Vahedifard et al., 2024). In parallel with the rapid expansion of the wildland-urban interface, post-fire geohazards pose a significant threat to the well-being and integrity of communities and critical infrastructure (Burke et al., 2021; Cannon and DeGraff, 2009; De Graff, 2014). The shift in wildfire elevation to higher altitudes has especially increased the chance of post-fire rainfall-triggered landslides and debris flows (AghaKouchak et al., 2018; Alizadeh et al., 2020, 2023). Post-fire landslides have been observed and documented in several studies (e.g., Benda and Dunne,

* Corresponding author at: Department of Civil and Environmental Engineering, Tufts University, Medford, MA 02155, USA.
E-mail addresses: Masood.Abdollahi@Terracon.com (M. Abdollahi), farshid.vahedifard@tufts.edu (F. Vahedifard), ben.leshchinsky@oregonstate.edu (B.A. Leshchinsky).

https://doi.org/10.1016/j.enggeo.2024.107538
Received 15 June 2023; Received in revised form 1 April 2024; Accepted 29 April 2024
Available online 30 April 2024

1997; Campbell, 1975; Gehring et al., 2019; May and Gresswell, 2004; Peduto et al., 2022). These observations highlight the imperative for further research to enhance our understanding and susceptibility mapping of post-fire rainfall-triggered landslides. The findings of such studies can contribute toward developing more accurate and effective strategies for assessing and mitigating the risks associated with such landslides.

Shallow landslides and debris flows are common hazards in mountainous terrains worldwide. While the triggering factor is commonly precipitation, wildfire can predispose burned areas to different forms of instability. With increased urbanization in mountainous regions, a more detailed understanding of the process that controls the shallow landslides following a wildfire is critical. Regional susceptibility maps and models are generally used to investigate post-wildfire ground instabilities' temporal and spatial distribution. Over the last few years, several techniques have been adopted for post-wildfire landslide or debris-flow susceptibility mapping. Almost all these techniques belong to the following categories: qualitative or heuristic methods and quantitative or semi-quantitative methods (He and Beighley, 2008; Melo and Zêzere, 2017). Heuristic methods are based on prior knowledge and experience of post-fire ground failures. They involve geomorphological analysis and indexing factors contributing to slope instability and ranking them based on their impact (e.g., Carabella et al., 2019).

Quantitative and semi-quantitative methods encompass deterministic approaches, typically employed at a slope scale, as well as statistical approaches such as machine learning and logistic regression. The latter includes the development of empirical models using historical observations of post-fire rainfall-induced slope instabilities in the relevant region (Cannon et al., 2010; Donovan and Santi, 2017; Gartner et al., 2008; Di Napoli et al., 2020). Empirical models are typically computationally efficient and can, therefore, be pivotal for conducting rapid hazard analyses. They are particularly adept at establishing rainfall intensity-duration thresholds for burned areas, offering quick, preliminary estimates of mass wasting susceptibility post-wildfire, and sidestepping the computational demands of process-based models. Importantly, these models can be integrated into Geographic Information Systems (GIS) for evaluating post-fire geohazards, crucial for emergency management. For instance, in southern California, empirically derived thresholds are integral to post-fire debris-flow early warning systems (Staley et al., 2017). However, these models are region-specific and only applicable to the narrow geographical locations and specific geologic, geomorphic, and climatic conditions by which they are trained. These models are data-driven, and in order to be used for other regions, they must be modified based on the characteristics of the new region of interest (Cannon et al., 2010). Empirical approaches established solely based on historical data exhibit a notable limitation by disregarding the impact of shifting precipitation patterns and fire regimes. This oversight becomes particularly significant as recent studies have indicated a growing occurrence of extreme precipitation events (Ragno et al., 2018). Finally, empirical models neither explicitly account for the wildfire-induced changes in land cover, soil properties, and near-surface processes nor consider the underlying physical processes leading to post-fire ground failures upon precipitation.

Wildfires can have short- and long-term effects on the mechanical and hydrological response of the affected area. Combustion of the above-ground biomass, intensive drying of the soil, decreases in the soil porosity and permeability, and enhancement or formation of a hydrophobic layer on the soil surface all lower the ground infiltration and enhance surface runoff after the fire (Chen et al., 2020; Debano, 2000; Ebel and Moody, 2020; Stoof et al., 2012). Depending on sediment and debris availability as well as geologic and topographic settings of the burned area, the increased runoff can lead to catastrophic debris flows shortly after the fire (Moody et al., 2013; Nyman et al., 2011; Rengers et al., 2016). However, during the recovery state after the fire and through the recovery of infiltration capacity, mass wasting tends to shift from runoff-driven failures like debris flows to infiltration-triggered discrete shallow landslides (Parise and Cannon, 2012). Roots decay, reduction of evapotranspiration, changes in vegetation coverage and canopy interception, and alteration in soil mechanical and hydraulic properties are key factors that predispose landscapes to shallow landslides following a wildfire (Gehring et al., 2019; Lei et al., 2022; Masi et al., 2021; Shakesby and Doerr, 2006; Vergani et al., 2017).

The main objective of this study is to develop a physics-based framework for regional shallow landslide susceptibility assessment of wildfire-disturbed areas. We employ an infinite slope stability model with a transient hydromechanical model to evaluate the safety factor of slopes over time following a wildfire. The proposed model is then employed in a GIS framework to account for the regional distribution of potential shallow landslides based on topography, geology, land cover, rainfall intensity and duration, and soil burn severity. The effect of wildfire on the hillslope behavior is seen through the induced changes in canopy interception, evapotranspiration rate, root reinforcement, and mechanical and hydraulic properties of the soil. The applicability of the proposed framework in post-wildfire landslide susceptibility mapping is tested against a case study in the San Gabriel Mountains, California, USA. The area experienced several landslides during a heavy rainstorm in January 2019, three years after it was burned in the San Gabriel Complex Fire in 2016.

2. Methodology

The proposed framework for mapping shallow landslide susceptibility post-wildfire comprises three components: 1) transient evaluation of soil moisture to analyze water flow in unsaturated, vegetated slopes; 2) a slope stability model to calculate the factor of safety; and 3) regional mapping to identify affected areas, burn severities, and variations in local rainfall patterns. This approach combines hydrological and geotechnical assessments with spatial analysis to effectively identify areas at risk of landslides following wildfire events. To the best of the authors' knowledge, this study is the first attempt in the literature to regionally examine the post-wildfire stability of variably saturated vegetated hillslopes against rainfall-triggered shallow landslides employing a physics-based approach. The formulations account for antecedent conditions of soil and vegetation cover, wildfire-induced alterations in transpiration and root reinforcement, hydromechanical coupling, and time-varying infiltration rates. These new features distinguish the current study from prior studies in the field. It is noted that some of the elements integrated into the proposed framework are from well-established principles in the literature of unsaturated soil mechanics and hydrology. However, there has been no such attempt in the literature to integrate all these elements in one unifying framework and investigate thoroughly the post-wildfire stability of unsaturated hillslopes against rainfall-triggered shallow landslides in the form and details the current study has done.

2.1. Soil moisture dynamics

2.1.1. Soil water balance

The complete terrain soil water balance can be described as (Abbate et al., 2019; Daly and Porporato, 2006; Farmer et al., 2003):

$$\frac{\partial \theta}{\partial t} = P(t) - I_c(t) - LQ(T) - ET(t) \tag{1}$$

where θ is the soil volumetric water content, t is time, P is the rainfall rate, I_c is the canopy interception, LQ represents the sum of runoff and deep drainage below the root zone, and ET is the evapotranspiration rate.

Canopy interception is the amount of rainfall that remains on the leaf surface and depends on the canopy density, vegetation type, and rainfall intensity and duration (Kozak et al., 2007). Merriam (1960) developed the following model to estimate the cumulative interception during each

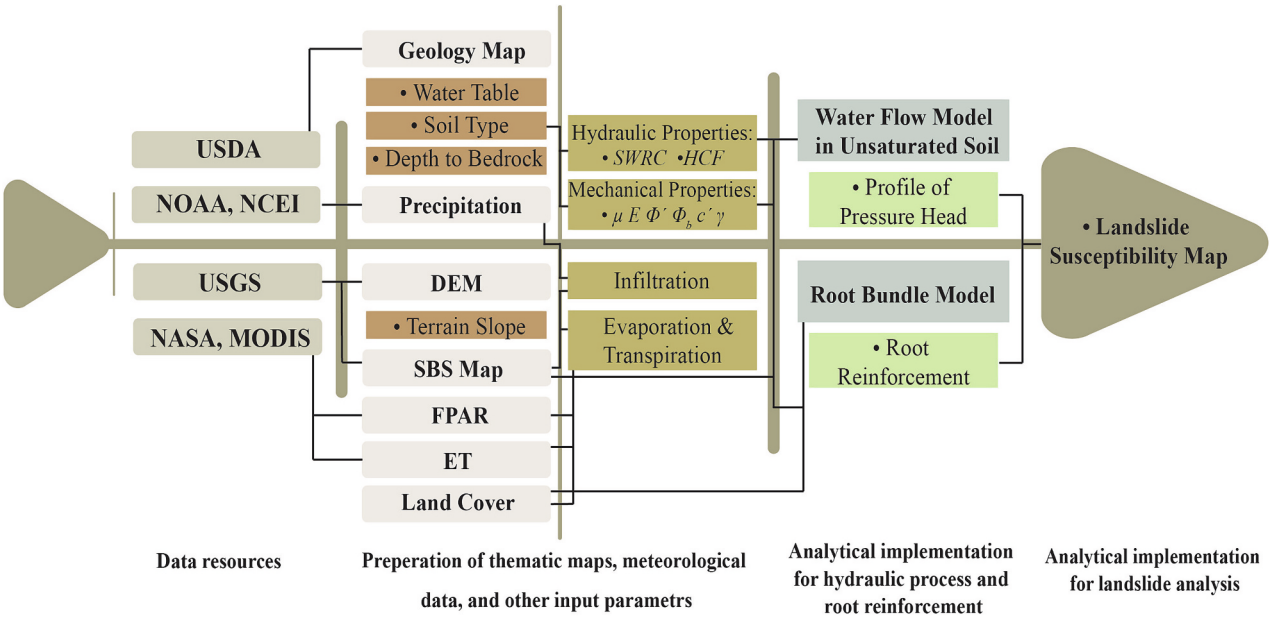

Fig. 1. Flowchart of the proposed regional susceptibility mapping of post-wildfire landslides.

rainfall event:

$$I_c = S^c_{max}\left(1 - e^{-\frac{P}{S^c_{max}}}\right) \tag{2}$$

where S^c_{max} is the canopy's maximum storage capacity across the study area, assuming complete canopy cover. This equation was originally developed for forests with complete area coverage. However, for sparse canopy vegetation such as crops and shrubs, the Merriam model is modified as follows (Aston, 1979; Kozak et al., 2007):

$$I_c = F_c S^c_{max}\left(1 - e^{-\frac{\eta P}{S^c_{max}}}\right) \tag{3}$$

$$\eta = 0.065LAI \tag{4}$$

where F_c is the canopy cover fraction within the modeling unit (i.e., grid cell or pixel), η equals the fraction of rainfall that falls on the canopy, and *LAI* is the leaf area index defined as the amount of leaf material in a canopy. *FPAR*, defined as the fraction of incoming solar radiation absorbed by a photosynthetic organism, is used as a surrogate of vegetation fraction (F_c) in this study (Los et al., 2000). The canopy's maximum storage capacity can be evaluated using different datasets or empirical equations (e.g., von Hoyningen-Huene, 1981).

It is assumed that runoff and drainage into deeper layers occur instantly when the layer is close to saturation (Bouten and Jansson, 1995). The two mechanisms that generate runoff are soil saturation and Hortonian overland flow during the rainfall. The coefficient of infiltration (α) is used in this study to calculate the amount of water that infiltrates the soil from rainfall that reaches the ground, $P_g(t)$.

$$I(t) = \alpha \times P_g(t) \tag{5}$$

where I is the amount of rainfall that infiltrates into the soil. This study does not model the redistribution of the runoff water from one grid cell to the adjacent cells at lower elevations.

ET data are collected using the *MODIS MOD16* global evapotranspiration product with a spatial resolution of 500 m and a temporal resolution of 8 days. The *MOD16 ET* datasets are calculated based on the improved *ET* algorithm proposed by Mu et al. (2011) over their older version model (Mu et al., 2007). The algorithm is a modification of the Cleugh et al., 2007 model and is based on the Penman-Monteith logic (Monteith, 1965). The algorithm employs *MODIS* land cover, albedo, *LA*, Enhanced Vegetation Index (*EVI*), and daily meteorological data from NASA's Global Modeling and Assimilation Office (Mu et al., 2011). The evapotranspiration rate can be proportioned into evaporation (E) and transpiration (T) based on the vegetation cover fraction (Mu et al., 2011):

$$\mathrm{T} = ET \times F_c \tag{6}$$

$$E = ET \times (1 - F_c) \tag{7}$$

2.1.2. Water flow in unsaturated slopes

The flow of water into an unsaturated vegetated slope is modeled by extending (Richards, 1931) equation. The one-dimensional form of Richards' (1931) equation to describe the water flow in the vertical (Z) directions is defined as:

$$\frac{\partial}{\partial Z}\left[k\left(\frac{\partial h}{\partial Z} + 1\right)\right] = \frac{\partial \theta}{\partial t} \tag{8}$$

where k is the hydraulic conductivity of the soil and a function of its moisture content, and h is the pressure head. Considering the slope inclination (β), and the effect of transpiration on water flow in vegetated slopes, Eq. (8) can be modified for the direction perpendicular to the slope ($z = Zcos\beta$) as follows:

$$\frac{\partial}{\partial z}\left(k\frac{\partial h}{\partial z}\right) + \frac{\partial k}{\partial z}cos\beta - S(z) = \frac{\partial \theta}{\partial t} \tag{9}$$

$$S(z) = A_r(z)TH(z) \tag{10}$$

where $S(z)$ is the sink term considering the effects of root water uptake, $H(z)$ is the Heaviside function equal to 1 for the root zone and 0 beyond the root depth, and $A_r(z)$ is a shape function describing the root distribution along the depth. In this study, it is assumed that roots are distributed uniformly along the soil depth.

Water flow in the soil is a coupled phenomenon (Khalili et al., 2008; Thomas and He, 1997). Water flux in and out of the soil changes the soil's effective stress, which causes soil deformation. These changes, in turn, affect water flow in the soil media by altering the soil porosity, permeability, and water retention capacity (Wu and Zhang, 2009). Considering this coupled behavior, Eq. (9) can be rewritten as (Tracy and Vahedifard, 2022, 2023):

$$\frac{\partial}{\partial z}\left(k\frac{\partial h}{\partial z}\right)+\frac{\partial k}{\partial z}cos\beta-S(z)=S_e\chi\gamma_w\frac{(1+\upsilon)(1-2\upsilon)}{(1-\upsilon)E}h+(\theta_s-\theta_r)\frac{\partial S_e}{\partial t} \quad (11)$$

where χ is the Bishop (1959) effective stress parameter and E is the soil elastic modulus. They are both functions of soil moisture content and are obtained through an iterative process. θ_s and θ_r are the saturated and residual water contents, respectively. S_e is the effective degree of saturation and can be calculated as:

$$S_e=\frac{\theta-\theta_r}{\theta_s-\theta_r} \quad (12)$$

The complete derivation of Eq. (11) can be found in Abdollahi et al. (2023) and (Tracy and Vahedifard, 2022, 2023). Eq. (11) is inherently nonlinear. To linearize and solve the equation, we took the following steps and assumptions:

1. The exponential functional model of Gardner (1958) is used to describe the soil water retention curve (SWRC) and the hydraulic conductivity function (HCF):

$$k=e^{\alpha h}k_s \quad (13)$$

$$S_e=e^{\alpha h} \quad (14)$$

where α is a fitting parameter.

2. The following change of variables is used:

$$\overline{h}=e^{\alpha h}-e^{-\alpha cos\beta z} \quad (15)$$

$$\widehat{h}=\overline{h}-\overline{h_{ss}} \quad (16)$$

where $\overline{h_{ss}}$ is the steady-state solution to Eq. (11) using the first change of variables (Eq. (15)).

3. Eq. (11) can be solved for a specified head pressure at the top boundary (h_{top}). To solve the equation for a given water flux at the top boundary (q), an iterative procedure is employed to find the corresponding pressure head for a given $q(t)$.

The solution to Eq. (11) can be obtained as follows:

$$\overline{h_{ss}}=\begin{cases} c_2-\dfrac{e^{-\alpha z\mathrm{Cos}\,\beta}c_1 sec\,\beta}{a} & H(z)=0 \\ \dfrac{\alpha k_s c_2+(\alpha S(z-L_1)-e^{-\alpha z cos\,\beta}k_s c_1)sec\beta+S\left(-1+e^{-\alpha(z-L_1)cos\beta}\right)sec^2\beta}{\alpha k_s} & H(z)=1 \end{cases} \quad (17)$$

$$c_2=\frac{\left(e^{\alpha h_{top}}-e^{-\alpha Lcos\beta}\right)-\frac{SL_2}{k_s cos\beta}+\frac{S}{\alpha k_s cos^2\beta}-\frac{Se^{-\alpha L_2 cos\beta}}{\alpha k_s cos^2\beta}}{1-e^{-\alpha Lcos\beta}} \quad (18)$$

$$c_1=c_2\times\alpha\times cos\beta \quad (19)$$

$$\widehat{h}=\sum_{k=1}^{\infty}A_k sin(\lambda_k z)exp\left(-\frac{\alpha cos\beta}{2}z-\frac{\left(\lambda_k^2+\frac{\alpha^2 cos^2\beta}{4}\right)}{\chi\gamma_w\frac{(1+\nu)(1-2\nu)}{E(1-\nu)}+\alpha(\theta_s-\theta_r)}k_s t\right) \quad (20)$$

$$\lambda_k=\frac{\pi k}{L}\ k=0,1,2,\ldots \quad (21)$$

where A_k is a constant that can be evaluated from the initial condition ($\widehat{h}(z,0)=-\overline{h}_{ss}$). The detailed derivation of Eqs. (17)–(21) is presented by Abdollahi et al. (2023).

The calculated pressure head solution is introduced into a Heaviside series expansion to describe a time-varying flux (i.e., infiltration or evaporation) at the top boundary:

$$h(z,t)=\sum_{n=1}^{N}H(t-t_n)\times\left(h(z,t-t_n)|_{q_n}\right)-\sum_{n=1}^{N}H(t-t_{n+1})\times\left(h(z,t-t_{n+1})|_{q_n}\right) \quad (22)$$

where N is the total number of time intervals, t_n is the time at the n^{th} time interval in the top boundary surface flux sequence, and q_n is the surface flux at the n^{th} time.

A new feature of the current study lies within employing a coupled hydromechanical model of unsaturated soils that considers fluid-solid interactions, a critical factor often overlooked in many other analytical models designed for shallow landslide prediction. The choice, albeit with its simplifications, is a step forward in understanding these complex phenomena under the veil of uncertainty. Recent studies (Tracy and Vahedifard, 2022, 2023) have demonstrated significant differences in pressure heads obtained from coupled versus uncoupled analytical solutions for fine-grained soils with a low Gardner's coefficient. Their findings indicate that uncoupled solutions reach a steady state faster than coupled models in such soils, revealing the considerable impact of hydromechanical coupling. This effect diminishes as Gardner's coefficient increases, highlighting the importance of considering hydromechanical coupling in landslide modeling.

2.2. Infinite slope stability

Shallow landslides are most frequently translational slope failures involving the upper few meters of unconsolidated surface materials such as soil or regolith (Godt et al., 2012). In this paper, slope stability is examined using a one-dimensional infinite slope stability model (Taylor, 1948). The infinite slope method is ideal for landslides in which the failure and ground surfaces are near-parallel, the slide's thickness-to-length ratio is relatively small, and the local topographic curvature is minor (Milledge et al., 2012). Many studies have shown that this mechanism can reasonably represent shallow landslides in mountainous terrain, including those disturbed by wildfire (e.g., Gorsevski et al., 2006; Godt et al., 2012; Araújo Santos et al., 2020). However, future work could consider different failure mechanisms through the adaptation of different slope stability methods that reflect appropriate landslide kinematics (e.g., rotation, compound failures, etc.).

In the infinite slope method, the slope's factor of safety is defined as the ratio of basal Coulomb friction to gravitationally-induced downslope destabilizing shear stress. Including the contribution of soil suction and root reinforcement (c_ψ *and* c_r), the factor of safety, F_S, along the z direction is defined as (Baum et al., 2010; Zhang et al., 2014):

$$F.S.=\frac{c'+c_r-c_\psi}{\gamma_s(L-z)sin\beta}+\frac{tan\phi'}{tan\beta} \quad (23)$$

where γ_s is the unit weight of soil, and L is the total thickness of the soil layer. c_ψ can be estimated using different shear strength models. In this study c_ψ is defined as (Fredlund and Rahardjo, 1993):

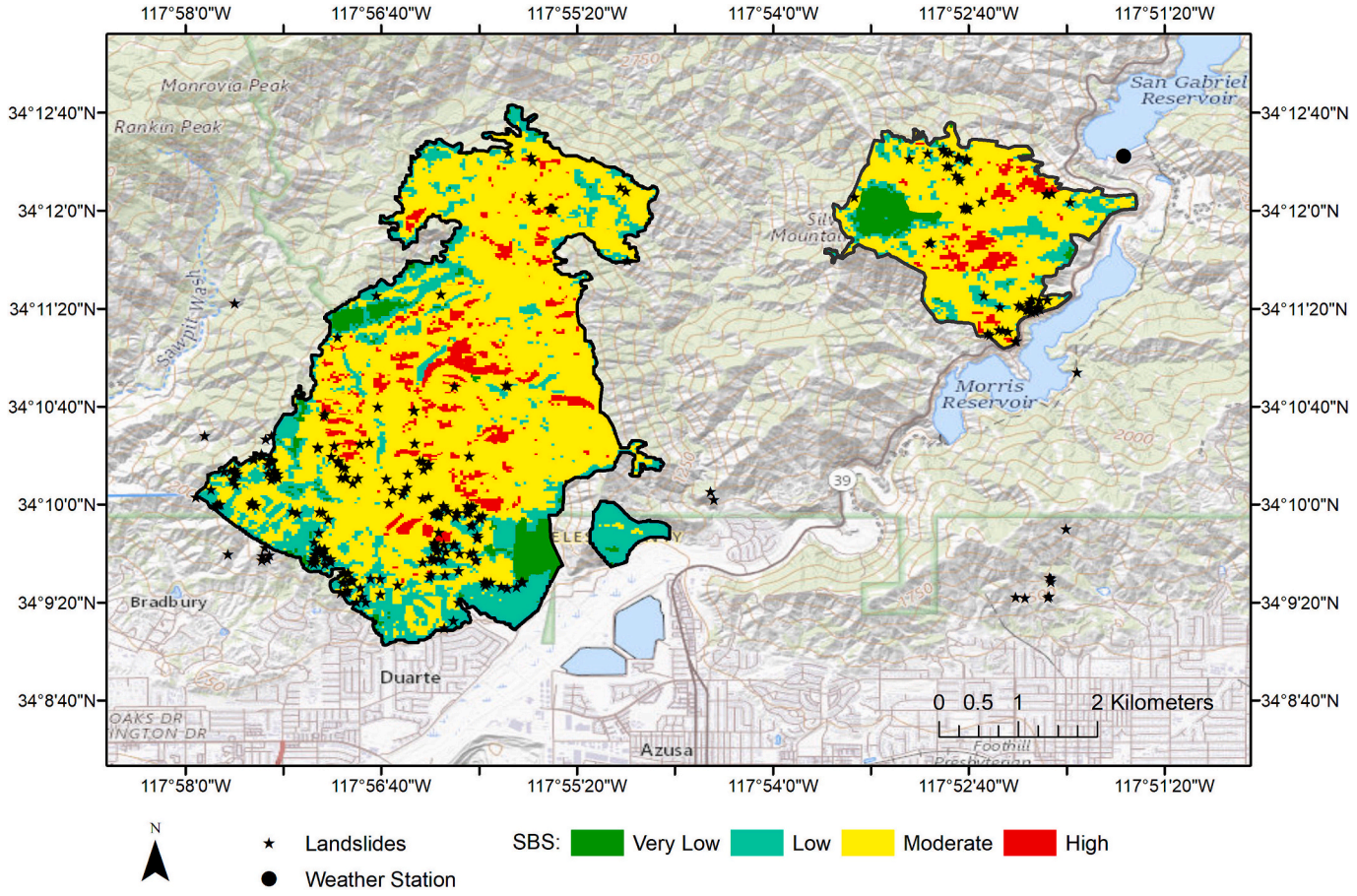

Fig. 2. Location of the study area in Southern California, thematic map of the San Gabriel Complex Fire *SBS*, location of landslides, and the weather station.

$$c_\psi = h(z,t)tan\phi^b \tag{24}$$

where ϕ^b represents the rate of increase in shear strength relative to the matric suction. Root reinforcement (c_r) is considered based on landcover type and is simplified as a cohesion as limited information regarding load-displacement behavior and vegetation density is available at the scales of interest, an assumption common in many studies (e.g., Schmidt et al., 2001; Wu et al., 1979; Zhuang et al., 2022).

2.3. Regional mapping

Fig. 1 illustrates the key components of the proposed framework. The post-fire landslide susceptibility mapping consists of 3 stages. The first step is to prepare the data grids of the area geology, digital elevation model (*DEM*), land cover and fraction of photosynthetically active radiation (*FPAR*), soil burn severity (*SBS*), and meteorological data including precipitation and evapotranspiration (*ET*). These data can be obtained from different resources. However, in this study, the soil survey geographic database (*SSURGO*) provided by the United States Department of Agriculture (*USDA*), National Centers for Environmental Information (*NCEI*) data archives, the United States Geological Survey (*USGS*) databases, and *NASA MODIS* (a satellite-based sensor for earth measurements) are used to obtain the required data. In the second phase, a grid-based distributed analytical model of unsaturated slope stability is implemented using *Python* and *ArcGIS* programs. The spatial distribution of the model is captured by discretizing the area into consistent grid cells for which the input data are obtained from the raster layers and records. Such data are used in calculating canopy interception, water flow in unsaturated soils, and root reinforcement. Profiles of pressure head across the disturbed area are calculated using the hydromechanical model of water flow in unsaturated soil discussed in the previous sections. Finally, a factor of safety of cells is assessed, and the areas susceptible to landslides are mapped across the burned area at the spatial resolution of 10 m.

3. Study area

The study area is located at the front range of the San Gabriel Mountains in the vicinity of the San Gabriel River and was burned by the San Gabriel Complex Fire. The San Gabriel Complex Fire was the combination of two separate wildfires, the Fish Fire and the Reservoir Fire, both of which ignited on June 20th, 2016, and burned parts of the Angeles National Forest located within Los Angeles County in Southern California. The fire was contained on July 23rd, 2016, after it had burned an area of 22 km^2 (CAL FIRE, 2022). Fig. 2 shows the location, perimeter, and soil burn severity of the fire. The study area has a Mediterranean and sub-tropical climate with rainy winters and dry summers (Rulli and Rosso, 2005). Based on climatic data for the 30 years between 1991 and 2020, the annual average precipitation for the area is 720 mm, most of which (620 mm) occurs in Winter and Spring (NCEI, 2023). Vegetation cover is predominantly shrubs and grass (Rulli and Rosso, 2005; Terwilliger and Waldron, 1991). Roots are mostly present within the soil mantle. However, they also can deeply penetrate the weathered bedrock ($\geq 4\ m$), and are largely confined to the joint traces (Sternberg et al., 1996). However, they can penetrate and extend into the underlying weathered bedrock (Rengers et al., 2020).

The study area is part of the Transverse Ranges consisting of Mesozoic granitic rocks, and Precambrian igneous and metamorphic rock complexes. There are also a few Pleistocene non-marine sedimentary layers near riverbeds. Steep slopes with shallow soils in this region result

from a fast tectonic uplift caused by the collision of tectonic plates over 6 million years ago (Bull, 1991; DiBiase et al., 2010). The soil thickness in the area barely exceeds 1 m on hillslopes, and according to the *USDA* datasets (2022) can mostly be graded as sand or loam with high permeabilities (Tang et al., 2019). The area is prone to landslides due to its steep slopes and extreme rainfall events that periodically fall over the region (Campbell, 1975). However, wildfires have increased the likelihood of instability in this region. In the Las Lomas watershed within the Fish Fire's perimeter, 11 debris flows were observed during the first rainy season following the fire (Tang et al., 2019). According to Rengers (2020), the third rainy season after the fire initiated widespread shallow landsliding in the area. San Gabriel Complex Fire had a landslide density of 11.8 landslide scars per square kilometer and tangent of angle of reach (ratio of landslide's change in vertical height from its scarp to its toe and runout length) of <0.5 to 1.5 (Rengers, 2020). Observations showed that >90% of these landslides were located within the boundaries of the San Gabriel Complex Fire.

Python (version 3.7) and ArcGIS (version 10.8) were utilized to develop a grid-based, distributed analytical model for the study area's variably saturated soils. This model, designed to solve soil moisture and infinite slope stability equations, aids in mapping susceptibility to post-wildfire, rainfall-induced shallow landslides. The model's spatial discretization was achieved by dividing the research region into grid cells with a size of 10 m, which resulted in 209,090 and 57,078 cells for the Fish Fire and Reservoir Fire, respectively.

The soil burn severity map was obtained from the USGS Burn Severity Portal, Burned Area Emergency Response (BAER, 2022) with a resolution of 30 m (Fig. 2). These maps are created using the differenced normalized burn ratio (*DNBR*) approach using the archived and current Landsat imagery. The *DNBR* values are then categorized into very low, low, moderate, and high burn severities and shown on a Burned Area Reflection Classification (*BARC*) map (Clark et al., 2006). According to the *SBS* map, 74% and 76% of the land burned in the Fish Fire and Reservoir Fire, respectively, have moderate to high burn severity.

The locations of the landslides were mapped using an inventory created by (Rengers, 2020) (Fig. 2). This dataset contains 286 landslide polygons mapped after a rainstorm on 16–17 January 2019. Out of 286 landslides, 264 landslides are located within the perimeters of the San Gabriel Complex Fire.

The daily rainfall data (Fig. 3) was received from *NOAA*, *NCEI* online database (2022) for a weather station located at the San Gabriel Dam (34° 12′ 18.72", - 117° 51' 38.88") (Fig. 2). The weather station is in 1.8 and 7.6 km distances from the centers of Reservoir and Fish Fires, respectively. The total rainfall reaching the ground was calculated using Eqs. (3) & (4). From this value, the amount that would infiltrate the soil was estimated via Eq. (5). Considering the high permeability of the colluvial deposits in the study area compared to the typical rainfall intensity, the coefficient of infiltration is set to 1.0 based on the high permeability of the soil type in the study area. *ET* is collected using *MODIS* Global Terrestrial Evapotranspiration Product (Gap-filled MOD16A2GF) in 500 m resolution with a temporal resolution of 8 days. *FPAR* and *LAI* are extracted from the *MODIS* datasets (MOD15AH2) with a spatial resolution of 500 m. Due to the coarser resolution of the *MODIS* data, the data are down-sampled to 10 m grid cells.

The terrain slope was calculated from the digital elevation model (*DEM*) with a resolution of 1 m provided through the 3D elevation program by *USGS* (2022) (Figs. 4a & 4b). Within the boundaries of either of the two fires, slopes have a median value of 41° and a standard deviation of 11°. The *DEM* resolution is finer than the grid size we used to discretize the area. For each grid, the representative slope is the mean value of the finer pixels' inclination value. Figs. 4c & 4d show the soil map of the area created using the *SSURGO* database (2022). As seen, the majority of the soil texture in the area can be classified as either loam (*CL*) or sandy loam (*SC*), which agrees with prior findings and observations (Thomas et al., 2021). The soil cover in the area is relatively shallow. Using the *SSURGO* database (2022), it was found that soil thickness barely exceeds 50 cm. Investigating the landslide characteristics, (Rengers, 2020) indicated that the landslides generally had depths ranging between 0.15 and 0.50 m and occurred at the interface of soil and the underlying saprolite. (McGuire et al., 2019) also reported that the soil in the study area is generally thin, rarely exceeding 1.0 m. In this study, it was found that the soil thickness for the majority of the analyzed grids is approximately 0.5 m.

The area land cover (Figs. 4e & 4f) was obtained from the Terra and Aqua combined Moderate Resolution Imaging Spectroradiometer (*MODIS*) Land Cover Type (MCD12Q1). The data is available in a spatial resolution of 500 m. The dominant vegetation types of the area are grass and shrubs. This also can be confirmed with prior studies that defined

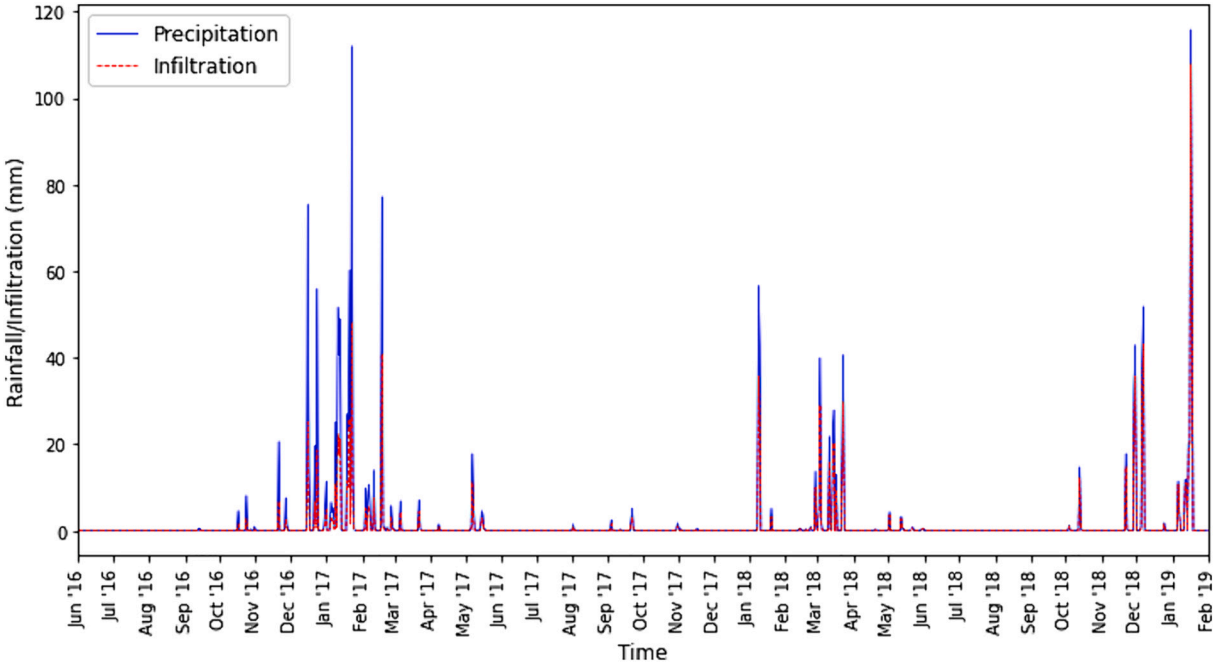

Fig. 3. Daily rainfall data from the San Gabriel Dam rain gauge station in the study area and the calculated infiltration rate.

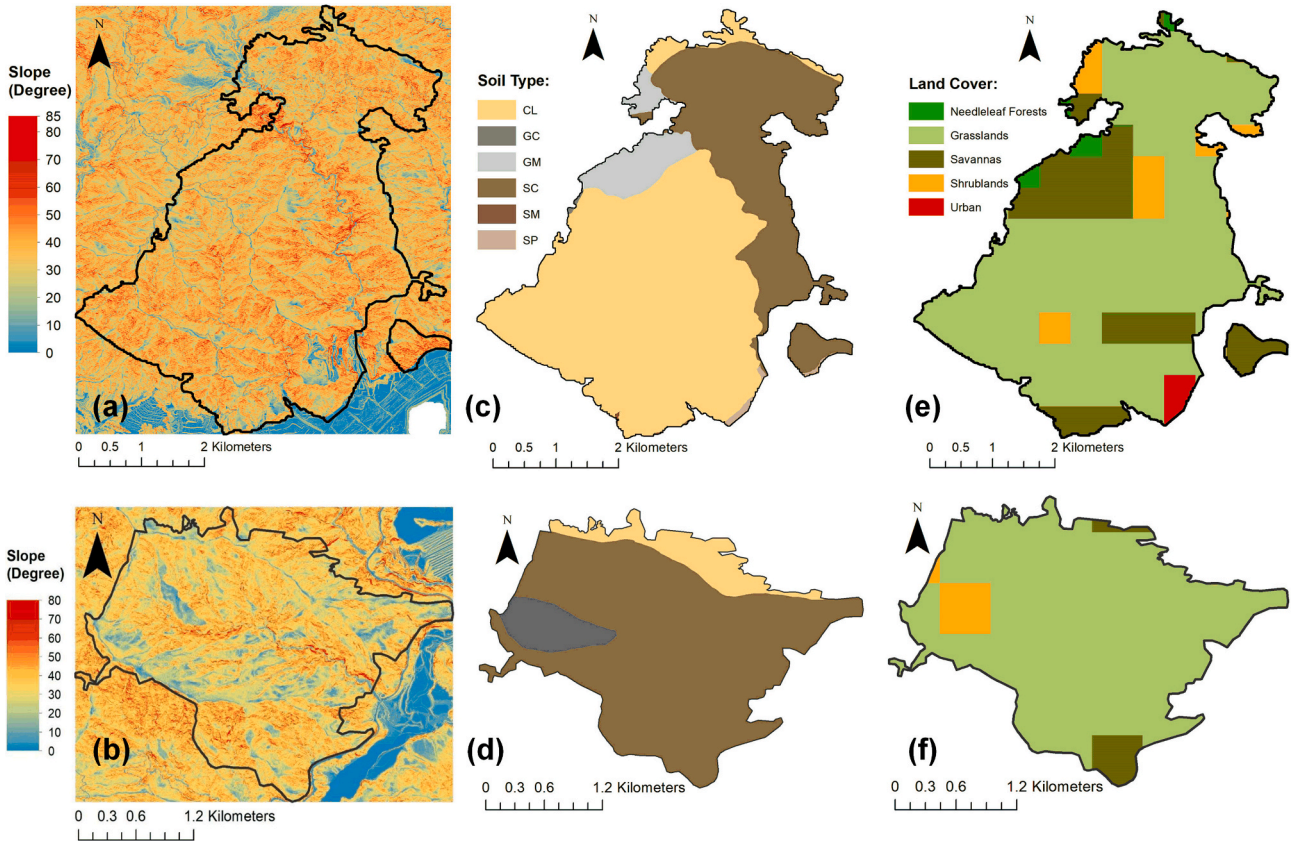

Fig. 4. a) slope angle, c) soil type, e) land cover within boundaries of the Fish Fire; b) slope angle, d) soil type, f) land cover within boundaries of the Reservoir Fire.

grass and different species of shrubs and bushes, usually known as chaparral, as the dominant vegetation type of the area (Rulli and Rosso, 2005; Terwilliger and Waldron, 1991). Depending on the vegetation, measured parameters for the main land cover types in North America gathered by (Breuer et al., 2003) are used in this study to obtain the corresponding canopy's maximum storage capacity (S_c^{max}). (Terwilliger, 1988) did a comprehensive study on the contribution of roots of the different types of vegetation to the soil shear strength (c_r) in the study area. In the absence of more detailed data on the distribution of roots' physical and mechanical properties, these reported values are used in this study to evaluate the effect of root reinforcement on slope stability.

Table 1
Model parameters for soil and land cover properties for susceptibility mapping of 2019 shallow landslides.

PROPERTIES	VALUE			REFERENCES
Soil Type	CL	SC or SC-SM	SP	*USDA (SSURGO)*
ϕ' (°)	27	32	37	(Terwilliger and Waldron, 1991)
c' (kPa)	1.0	0.0	0.0	(Wohlgemuth and Hubbert, 2008)
α $(1/m)$	1.0	1.5	2.3	(Schaap et al., 2001)
$k_s(m/s)$	$1.4e-6$	4.4e-6	8.75e-5	(Schaap et al., 2001)
γ_s (kN/m^3)	17.1	17.1	16.4	(Terwilliger and Waldron, 1991)
Land Cover Type	Grass/ Savanna	Shrub	Needleleaf Forest	MODIS (MCD12Q1)
Root Reinforcement (kPa)	1.5	1.2	3.0	(Terwilliger, 1988)
S_c^{max} (mm)	1.7	1.1	2.2	(Breuer et al., 2003)

The proposed physics-based model was used to characterize changes in the factor of safety for each grid. The thematic maps and meteorological data obtained earlier were input to the water flow, root reinforcement, and slope stability models. Table 1 shows the input parameters of the properties of the different soil types and vegetation covers used in modeling. Based on the temporal resolution of the available data, we employed a time step of one day for the simulations. The model was run over the study area for a time period between 09/01/2018 to 01/31/2019 for three months. In general, due to the coarse nature of the soils in the study area, the changes in soil suction are rapid and mostly occur in response to precipitation. However, for a number of specific locations, the model was run from June 2016 to February 2019 to better illustrate the changes in the factor of safety following the fire and during different rainstorms. With respect to the infiltration measurements in the study area following the fire (Ebel and Moody, 2020; Tang et al., 2019), the coefficient of infiltration was reduced to one-third of its original value for areas burned at moderate to high severity (Abdollahi et al., 2023). Ebel and Moody (2020) conducted a study on fire's impact on soil hydraulic properties in Southern California, indicating that saturated hydraulic conductivity and sorptivity ratios between burned and unburned areas are approximately 0.37 and 0.36, respectively. Utilizing Philip's eqs. (1957, 1969) without adjustments for lateral spreading suggests a similar reduction in infiltration rates to about one-third of pre-fire levels. This finding aligns with post-wildfire observations by other studies (e.g., Conedera et al., 2003; Robichaud, 2000), confirming the consistency of these effects across studies. It is shown that rainfall with a return duration of one to two years can gradually wash away the fire-induced hydrophobic layer and improve the affected area's infiltration capacity (Abbate et al., 2019; Conedera et al., 2003; Robichaud, 2000). Following this approach, the coefficient of infiltration was increased by 0.1 following each rain event with

cumulative rain of >50 mm.

Wildfires can lead to a significant reduction in the number, tensile strength, and shear strength of roots and the soil-root system, with losses ranging from 50% to 80%, as documented in the literature (e.g., Gehring et al., 2019; Lei et al., 2022; Masi et al., 2021). The degradation of root reinforcement following wildfires is a well-recognized phenomenon (De Graff, 2018; Jackson and Roering, 2009; Vergani et al., 2017). However, a standardized method for assessing root recovery over time remains undeveloped. Studies have shown finer roots may lose strength more rapidly after fire compared to thicker roots (Lei et al., 2022). This might be because fine roots have a greater specific surface area and, hence, are more likely to be degraded by microorganisms in the soil following fire damage (Vergani et al., 2017). For the region considered in the current study, Rengers (2020) observed that areas burned five years before a storm had lower landslide density than those burned three years prior, attributing this to the longer period for vegetation and root reinforcement recovery, indicating a critical 3–5 year window for hydrologic and mechanical recovery. Qualitative indices based on surface conditions can be used to assess the roots' damage and loss (Parsons et al., 2010). Abdollahi et al. (2023) evaluated FPAR values and showed a three-year recovery window for vegetation regrowth in the study area. In the current study, the post-fire root reinforcement is reduced by 50% and

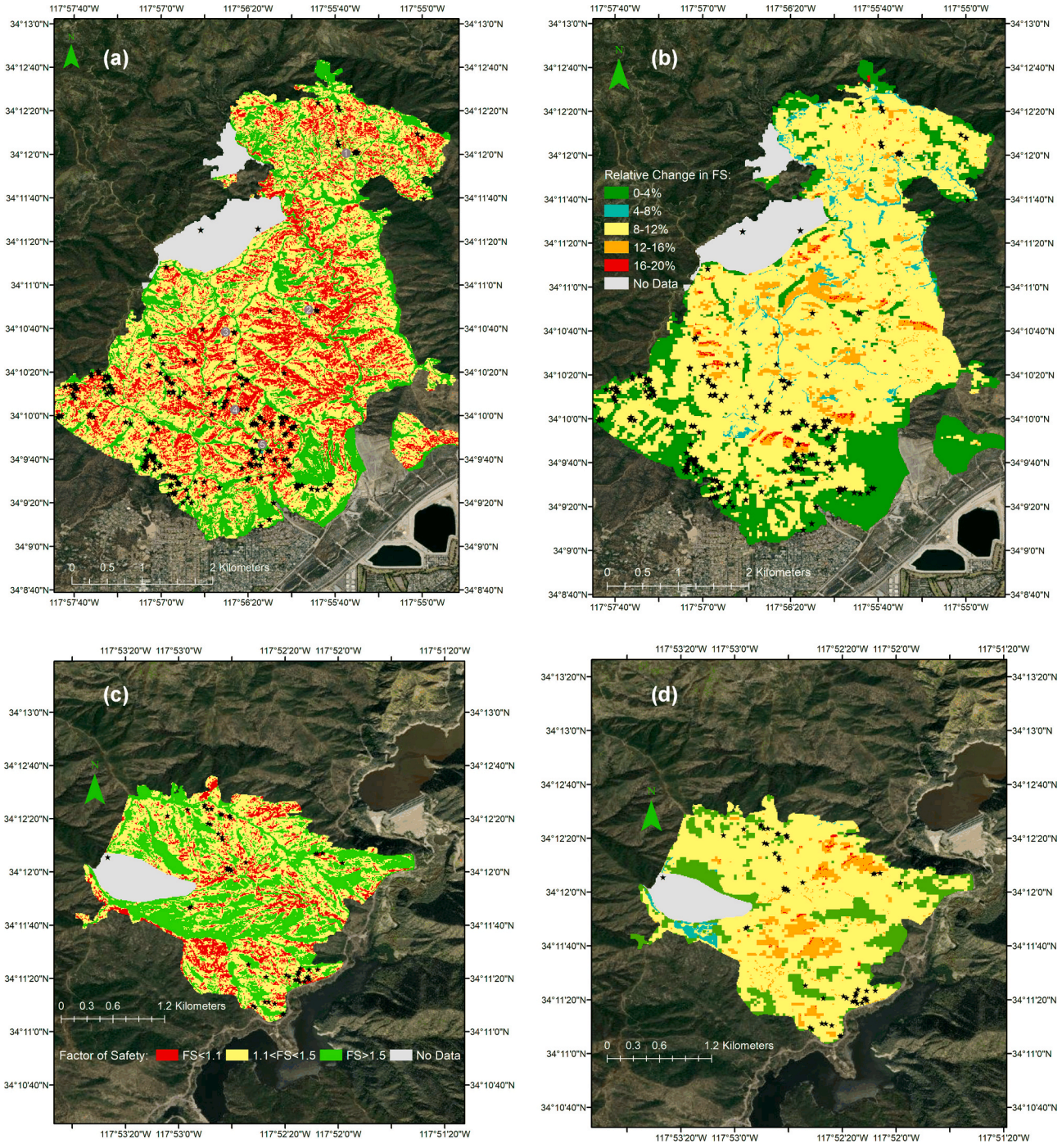

Fig. 5. Computed safety factors for slopes within a) the Fish Fire and c) the Reservoir Fire; Relative changes in factor of safety compared to no-fire scenario for b) the Fish Fire and d) the Reservoir Fire, Purple circles shown in subfigure (a) are cases for which changes in factor of safety is analyzed over a longer period of time. (For interpretation of the references to color in this figure legend, the reader is referred to the web version of this article.)

80% for moderate and high burn severity areas following wildfire, respectively. This assumption is likely conservative as it is expected that decay in root reinforcement may occur over time. However, some loss of roots from smoldering and incineration is likely as well and could support at least some near-immediate loss of root reinforcement following a wildfire. Further, this assumption at least provides quantitative bounds on the loss of stability stemming from loss of root reinforcement, particularly owing to the absence of field observations on the evolution of root behavior in these ecoregions, the multi-year window between the fire event, and the observed landslides, uncertainties in the vegetation type and its recovery time. The capability of the proposed model to more accurately predict the temporal risk of landsliding may significantly be improved by efforts to characterize temporal changes in root strength following wildfire.

We used coarse-resolution data on LAI, FPAR, and land cover across the burn area to assess the hydraulic and mechanical behavior of the soil in the years following a wildfire. Although the coarse resolution may limit the characterization in highly heterogeneous post-wildfire environments, the study area's prevalent grasslands, savannas, and shrublands, which typically do not undergo major post-wildfire vegetation type conversion, mitigate this concern. (Meng et al., 2014; Thomas et al., 2021).

In this study, we relied on limited existing data and vegetation indices to evaluate landscape recovery. We considered a consistent rise in the infiltration coefficient after its initial drop, acknowledging studies that reported an increase in soil hydraulic conductivity post-fire (Doerr et al., 2006; Raymond et al., 2020; Varela et al., 2015). The recovery process is influenced by various factors, including fire severity, disturbance history, post-fire land management, plant composition and regrowth, site geology, and climate throughout the post-fire years, necessitating site-specific assessments due to the heterogeneity in post-fire soil and hydrologic characteristics (Ebel et al., 2022; Wagenbrenner et al., 2021). Considering the complexities involved, a unified post-wildfire recovery trend cannot be defined for all sites. Instead, the post-wildfire recovery trajectories must be assessed on a case-by-case basis. Precise quantification of recovery trends across different landscapes and burn conditions is critical for assessing landslide hazards after wildfires in ecoregions where such trajectories have not been defined. However, this study presents a physics-based framework that would enable one to explore the evolving stability of shallow landslide-prone terrain following the fire, demonstrated through the assumptions posed herein that certainly could be refined as more data becomes available. Furthermore, the proposed framework can be integrated in a probabilistic manner as it can provide an objective estimate of the probabilistic stability of the slope even with incomplete or low-quality datasets, allowing a user to treat all inputs stochastically and provide valuable information for risk analyses.

4. Regional mapping of post-wildfire shallow landslides

The results of the analysis are illustrated in a post-wildfire shallow landslide susceptibility map (Figs. 5a & 5c). The factor of safety of 1.1 is considered as a threshold to separate unstable/marginally stable stability grids (shown in red color) from the stable grids. In particular, the model shows that 25% (4.5 km^2) and 15% (0.7 km^2) of the areas affected by the Fish and Reservoir Fires are at risk of landslide, respectively. The proposed model successfully captures locations of shallow landslides within regions deemed unstable, although it overpredicts areas prone to failure compared to the proposed inventory. When comparing true positives, the model showed an accuracy of 73%.

The model was also run for a no-fire scenario. In this case, all the inputs were the same except for the burn severity, which was set as "unburned". In this simulation, the land cover data and *ET* rate were obtained from a year prior to the fire (2015) in the same time period of the year for which the original model was run. The purpose was to better understand the extent to which wildfire could affect susceptibility (Figs. 5b & 5d). The comparison between the two scenarios shows that the landslides within the Fish Fire experience a median relative change of 10% in their factor of safety owing to the fire's effects. The same observation can be made for the Reservoir Fire where 95% of the landslides happened in regions experiencing a 3% to 16.5% reduction in their factor of safety, with a median reduction of 11%. Descriptive statistics of *SBS,* slope, soil type, and land cover for grids located within the observed landslides and the modeled unstable grids are summarized in Table 2.

The similarity between the modeled and observed landslides is more pronounced for the Reservoir Fire. This may be attributed to the smaller area affected by the fire and the more uniform distribution of the site properties and burn severity. Landslides generally occurred in regions with higher burn severities, steeper slopes, weaker soils, and areas where grass and shrubs were the dominant vegetation cover. In small areas across the affected region where soil deposits consisted of sand, gravel, or rock, or where the soil was covered by evergreen forests, almost no landslides were observed or modeled. Compared to the observed unstable slopes, the unstable regions captured by the model have steeper slopes and are mostly co-located where soil burn severity was moderate. For example, within the boundaries of the Fish Fire, 80% of the modeled unstable grids are burned at moderate burn severity and have a mean slope of 44°, while these values are 60% and 41° for all the grids within the observed landslides. This may explain the overprediction of the model in identifying slope failures in areas where no landslides were observed. One possible explanation is insufficient or

Table 2
Comparison between characteristics of observed and modeled unstable slopes.

	SBS		Slope (°)		Soil Type		Land Cover	
	Observed*	Model**	Observed	Model	Observed	Model	Observed	Model
Fish Fire	very low: 2% Low: 38% moderate: 60% severe: 0%	very low: 2% Low: 12% moderate: 80% severe: 6%	mean: 41 STD: 6 median: 41	mean: 44 STD: 4 median: 43	CL: 93% SC: 5% Others: < 2%	CL: 70% SC: 30%	grassland: 56% shrublands: 39% Savannas: 4% others: <1%	grassland: 56% shrublands: 39% Savannas: 4% others: <1%
Reservoir	very low: 0% Low: 10% moderate: 88% severe: 2%	very low: 3% Low: 10% moderate: 83% severe: 4%	mean: 39 STD: 5 median: 39	mean: 45 STD: 4 median: 44	CL: 3% SC: 97%	CL: 13% SC: 87%	grassland: 97% shrublands: 3%	grassland: 95% shrublands: 5%

* Observed in the grids located within the observed landslides.
** Observed in modeled unstable grids.

inaccurate data relating to triggered landslides at a finer scale. *SBS* is usually obtained within days following fire cessation. This may introduce inaccuracies. Finally, the most likely reason for overprediction, as is common in all physics-based models, is uncertainties with material properties at large scales and the coarse temporal and spatial resolution of input parameters.

The primary consequences of wildfire on shallow landslides are the removal of vegetation, decay of root strength, decrease in canopy interception, and decrease in infiltration capacity of the ground. Such changes affect soil strength and the flow of water over and through the soil, consequently governing the factor of safety of rainfall-triggered shallow landslides. For the five locations marked in Fig. 5a, we determined changes in the factor of safety and soil suction at the soil-bedrock interface from June 2016, post-wildfire, to January 2019, when widespread shallow landslides occurred (Fig. 6). The properties associated with these five points are summarized in Table 3.

Following the wildfire, there was a noticeable decrease in soil suction values, as depicted in Fig. 6b, likely due to diminished transpiration rates. This reduction was observed after each rainfall, with the most significant drop happening in the third year, aligning with the full recovery of soil infiltration capabilities. Specifically, Point 1 exhibited lower suction than the rest, a condition attributed to its slope being covered by coarser soil particles. The factor of safety (Fig. 6a) decreases significantly owing to wildfire-induced decreases in root reinforcement, root water uptake and the consequent decrease in soil suction. The following decreases in the factor of safety are associated with the three rainy seasons following the fire (Fig. 3). During the first rainstorm, no landslides were reported to occur in the study area. However, multiple debris flows were observed in the time window between 16 December 2016 and 18 February 2017 (Tang et al., 2019). This can be attributed to the significant drop in the ground infiltration capacity following the fire (Ebel and Moody, 2020; Tang et al., 2019), forcing the water to flow over the surface rather than infiltrate the soil. The accelerated overland flow, coupled with an increase in sediment generation, resulted in a series of debris flows. The increased sediment stems from different processes such as ravel, enhanced raindrop-driven sediment transport, or flow-driven sediment detachment. The second rainstorm was not

Table 3
Characteristics of individual studied slopes.

Point Number	SBS	Slope (°)	Soil Type	Land Cover	Soil layer Thickness (cm)
1	3	44	SC	Grassland	50
2	3	42	CL	Shrubland	50
3	3	43	CL	Shrubland	50
4	3	51	CL	Shrubland	50
5	4	44	CL	Grassland	50

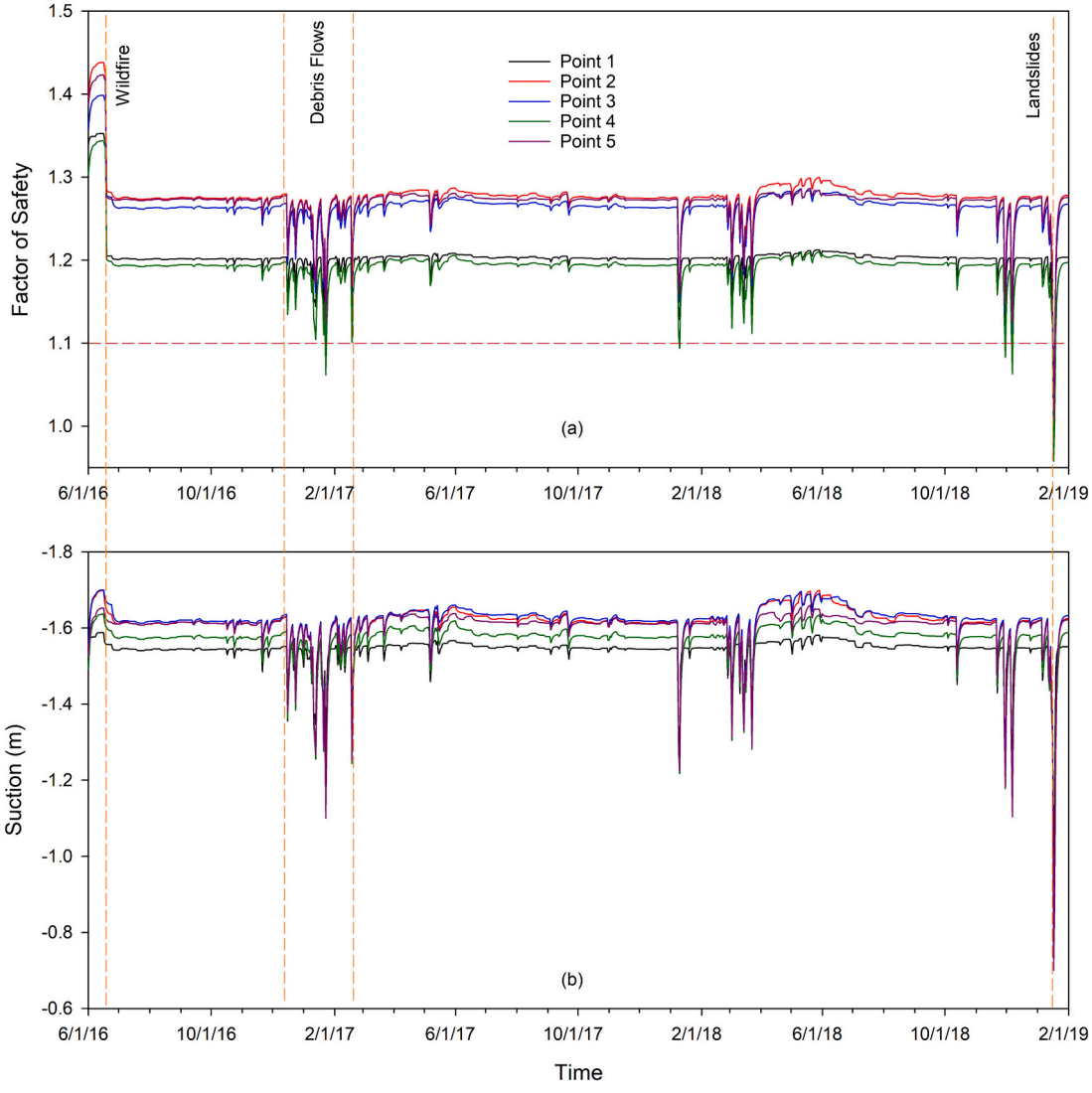

Fig. 6. Changes in a) factor of safety, b) suction of five selected slopes following the wildfire.

intense enough to generate landslides. At this point, the ground infiltration capacity is not fully recovered. Intense rainstorms in the third rainy season dropped the factor of safety of the slopes below 1.1. The model could capture the approximate timing of the landslide initiation on 17 January 2019 when a rainfall event of 115 mm in one day occurred over the area. Within the studied location, point 4 has the most sensitivity to rainfall events, attributed to the steep slopes in this location (mean slope of 51°). Point 5, which had severe soil burn severity, shows more rapid changes in the factor of safety compared to other locations. The lower factor of safety at point 5 compared to point 2 can be attributed to its steeper slope and higher burn severity, which resulted in a lower transpiration rate and more reduction to root reinforcement.

It is also observed that the factor of safety on sandy loam hillslopes is slightly more affected by fire compared to loamy hillslopes. Due to the shallow depth of the soil cover in the study area, soil cohesion is a strong control of slope stability. The effect of fire is slightly more pronounced in sandy loam, where cohesive strength sources from root reinforcement. Finally, no noticeable difference is observed between burned areas covered by grass or those covered by shrubs, potentially owing to similar root reinforcement of these vegetation types.

5. Sensitivity analysis: impact of root strength decay

The impact of wildfire on root strength and the subsequent rate of root strength loss were not directly measured, making these factors difficult to quantify. Given the shallow soil cover, roots play a crucial role in maintaining slope stability. In the absence of direct observations, we conducted sensitivity analyses to understand how variations in root reinforcement reduction post-fire affect safety factors and landslide susceptibility at five points of interest. Several previous studies (e.g., Sidle, 1991; Lei et al., 2022) suggest root strength declines exponentially post-mortem across different species. Therefore, we employed the following exponential function to model root strength attenuation over time post-wildfire:

$$c_r = cr_0 \times e^{-\omega t} \tag{25}$$

where c_{r0} is the initial root reinforcement before the fire, and ω is the empirical constant. For each location, we ran 1000 realizations for which ω were randomly assigned a value between 0 and 0.25 (root loss between 0 and 50% over 3 years) and 0–0.5 (root loss between 0 and 80% over 3 years) for moderately and severely burned slopes respectively. Box plots in Fig. 7 show the variation in the factor of safety of these five slopes upon January 2019 rainstorm for assuming different rates of root reinforcement loss. As seen, for all the cases examined, the median value of factor of safety falls below 1.1. A relatively low difference between the first and third quartile for all cases suggests low sensitivity of the results to the drop rate of the roots strength. As discussed before, the slopes were shallow and steep and on the verge of failure upon saturation, where slight changes in the root reinforcement could make them unstable. Slope 4 showed instability across all scenarios, attributed to its steep angle, making it insensitive to the rate of root strength loss. For the higher severity burned slopes (Point 5), the median factor of safety is considerably lower compared to other similar slopes (i.e., Points 1, 2, and 3). Finally, the sensitivity analysis showed that the probability of failure for Points 1, 2, 3, 4, and 5 were 58, 52, 78, 100, and 87%, respectively. The median factory of safety values for Slopes 1–5 shown in Fig. 7 largely coincide with the minimum factory of safety values observed in Fig. 6 for the January storm, suggesting that while decay is an important factor, these hillslopes were still sensitive to loss of vegetation and root reinforcement regardless of the timeframes of root decay.

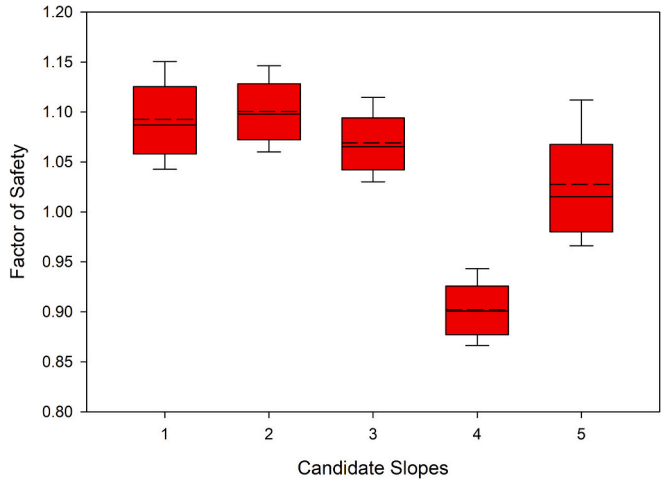

Fig. 7. Box plots for variation in factor of safety for the five selected slopes with variation in Root reinforcement loss rate.

6. Comparison of unburned and burned susceptibility

The results suggest that the wildfire had a significant impact on the stability of the slopes in the study area. Fig. 8a shows the frequency of the slopes' factor of safety for no-fire scenarios and the actual event where wildfire effects on soil and land cover properties were modeled. The two histograms are normalized to enable us to compare them better. It is seen that compared to the no-fire scenario, wildfire shifts the graph considerably to the left, where more areas are on the verge of failure. This is better shown in Fig. 8b, where the cumulative distribution of the two discussed histograms is displayed. Considering the factor of safety of 1.1 as the marginal stability limit, it is noted that wildfire has more than doubled the number of grids that fall below this value from 10% to 22%. These changes may seem modest, but are not trivial, especially as they relate to the frequency of fires in this ecoregion. These changes highlight why the effect of wildfire on susceptibility mapping of rainfall-triggered shallow landslides in disturbed areas must be considered.

7. Conclusions

This study presented a physics-based framework for analyzing the susceptibility of post-wildfire rainfall-triggered shallow landslides at a regional scale. The proposed solution incorporates soil burn severity mapping, geomorphological and land cover mapping, and meteorological data into a water flow model in unsaturated soil, a root bundle model, and an infinite slope stability equation to investigate the factor of safety of the fire-affected slopes. To account for the spatial distribution of the input parameters, the proposed model is employed in a *GIS* framework by discretizing the affected area into smaller grids where stability analysis is run for each grid. The presented solution is novel in the sense that it explicitly addresses the adverse effects of fire on soil properties, land cover and canopy interception, root reinforcement, and in general, on the surface and near-surface processes, which can lead to slope instability in rainy seasons following the fire. The model was used to map a series of detected shallow landslides in a 22.0 km^2 area located in the Angeles National Park in Southern California, which had been burned in the San Gabriel Complex Fire. The proposed model was successful in capturing both the timing and spatial distribution of the landslides with a positive accuracy of 73%. Landslides mostly occurred in regions where the soil was burned at moderate severity. The fire effect was more pronounced in sandy loam slopes where the soil cohesion is solely coming from the roots. Almost no landslides occurred in areas covered with needle-leaf evergreen forests where roots significantly improved slope stability. Out of the 286 shallow landslides, only two occurred in gravel and rocky slopes, which implies the main reason for the failures was the elimination of soil suction and its contribution to slope stability due to an increase in ground infiltration capacity during the recovery state of the area following the fire, and reduced

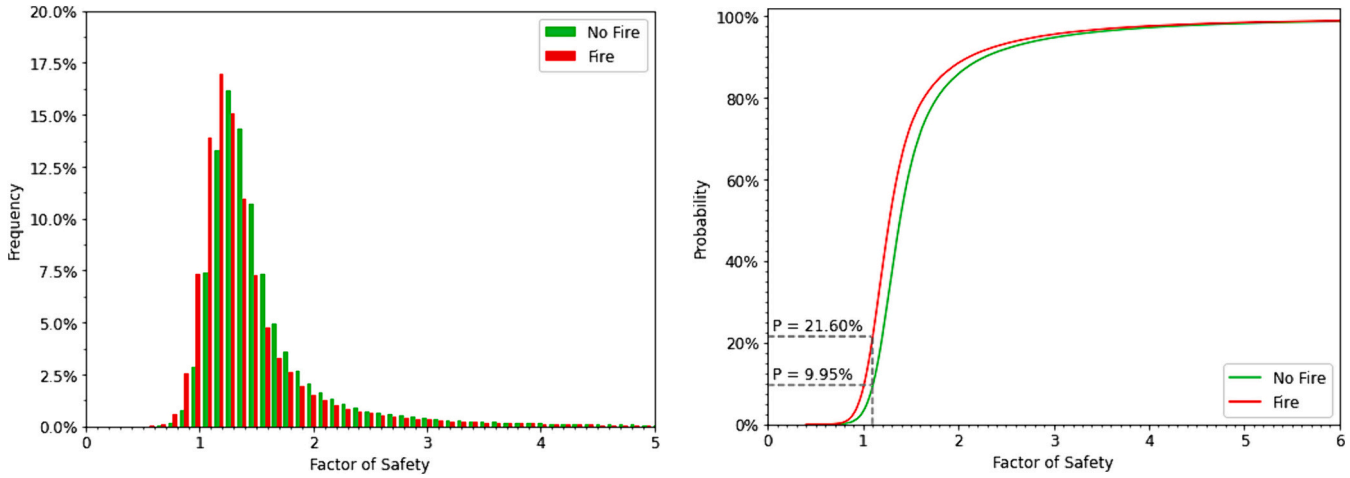

Fig. 8. Comparison between a) frequency and b) cumulative distribution probability of factor of safety of hillslopes in no-fire and fire-affected scenarios.

transpiration capacity of the roots. In conclusion, the model showed that compared to the no-fire scenario, a wildfire could double the number of unstable zones within the affected area. This work offers a methodological solution that assists the susceptibility mapping of post-wildfire landslide hazards, particularly in mountainous environments, that may be used to warn the communities at the wildland-urban interface of the danger of disastrous ground movements.

CRediT authorship contribution statement

Masood Abdollahi: Writing – original draft, Validation, Resources, Methodology, Investigation, Formal analysis, Data curation, Conceptualization. **Farshid Vahedifard:** Writing – review & editing, Visualization, Supervision, Resources, Project administration, Methodology, Investigation, Funding acquisition, Formal analysis, Conceptualization. **Ben A. Leshchinsky:** Writing – review & editing, Validation, Supervision, Software, Methodology, Investigation, Formal analysis, Conceptualization.

Declaration of competing interest

The authors declare that they have no known competing financial interests or personal relationships that could have appeared to influence the work reported in this paper.

Data availability

Data will be made available on request.

Acknowledgment

This material is based upon work supported by the National Science Foundation under Grant No. CMMI-1951636 and the United States Department of Agriculture (USDA), the National Institute of Food and Agriculture (NIFA) under Grant No. 2021-67022-35908.

References

Abatzoglou, J.T., Williams, A.P., 2016. Impact of anthropogenic climate change on wildfire across western US forests. Proc. Natl. Acad. Sci. 113 (42) https://doi.org/10.1073/pnas.1607171113, 11770 LP – 11775.

Abbate, A., Longoni, L., Ivanov, V.I., Papini, M., 2019. Wildfire impacts on slope stability triggering in mountain areas. Geosciences 9 (10), 417. https://doi.org/10.3390/geosciences9100417.

Abdollahi, M., Vahedifard, F., Tracy, F.T., 2023. Post-wildfire stability of unsaturated hillslopes against rainfall-triggered landslides. Earth's Future 11 (3). https://doi.org/10.1029/2022EF003213.

AghaKouchak, A., Huning, L.S., Chiang, F., Sadegh, M., Vahedifard, F., Mazdiyasni, O., et al., 2018. How do natural hazards cascade to cause disasters? Nature 561 (7724), 458–460. https://doi.org/10.1038/d41586-018-06783-6.

Alizadeh, M.R., Adamowski, J., Nikoo, M.R., AghaKouchak, A., Dennison, P., Sadegh, M., 2020. A century of observations reveals increasing likelihood of continental-scale compound dry-hot extremes. Sci. Adv. 6 (39) https://doi.org/10.1126/sciadv.aaz4571.

Alizadeh, M.R., Abatzoglou, J.T., Adamowski, J., Modaresi Rad, A., AghaKouchak, A., Pausata, F.S.R., Sadegh, M., 2023. Elevation-dependent intensification of fire danger in the western United States. Nat. Commun. 14 (1), 1773. https://doi.org/10.1038/s41467-023-37311-4.

Araújo Santos, L.M., Correia, A.J.P.M., Coelho, P.A.L.F., 2020. Post-wildfire slope stability effects and mitigation: a case study from hilly terrains with unmanaged forest. SN Appl. Sci. 2 (11), 1883. https://doi.org/10.1007/s42452-020-03660-8.

Aston, A.R., 1979. Rainfall interception by eight small trees. J. Hydrol. 42 (3–4), 383–396. https://doi.org/10.1016/0022-1694(79)90057-X.

Baum, R.L., Godt, J.W., Savage, W.Z., 2010. Estimating the timing and location of shallow rainfall-induced landslides using a model for transient, unsaturated infiltration. J. Geophys. Res. 115 (F3), F03013. https://doi.org/10.1029/2009JF001321.

Benda, L., Dunne, T., 1997. Stochastic forcing of sediment supply to channel networks from landsliding and debris flow. Water Resources Research 33 (12), 2849–2863. https://doi.org/10.1029/97WR02388.

BAER, 2022. Burned severity portal. Retrieved from https://burnseverity.cr.usgs.gov/baer/baer-imagery-support-data-download.

Bishop, A.W., 1959. The principle of effective stress. Teknisk Ukeblad 106 (39), 859–863.

Bouten, W., Jansson, P.-E., 1995. Water balance of the Solling spruce stand as simulated with various forest-soil-atmosphere models. Ecol. Model. 83 (1–2), 245–253. https://doi.org/10.1016/0304-3800(95)00102-2.

Breuer, L., Eckhardt, K., Frede, H.-G., 2003. Plant parameter values for models in temperate climates. Ecol. Model. 169 (2–3), 237–293. https://doi.org/10.1016/S0304-3800(03)00274-6.

Bull, W.B., 1991. Geomorphic Responses to Climatic Change. Oxford University Press, New York, NY (United States).

Burke, M., Driscoll, A., Heft-Neal, S., Xue, J., Burney, J., Wara, M., 2021. The changing risk and burden of wildfire in the United States. Proc. Natl. Acad. Sci. 118 (2), e2011048118 https://doi.org/10.1073/pnas.2011048118.

Campbell, R.H., 1975. Soil slips, debris flows, and rainstorms in the Santa Monica Mountains and vicinity, southern California. Profess. Pap. https://doi.org/10.3133/pp851.

Cannon, S.H., DeGraff, J., 2009. The increasing wildfire and post-fire debris-flow threat in Western USA, and implications for consequences of climate change. In: Landslides – Disaster Risk Reduction. Springer Berlin Heidelberg, Berlin, Heidelberg, pp. 177–190. https://doi.org/10.1007/978-3-540-69970-5_9.

Cannon, S.H., Gartner, J.E., Rupert, M.G., Michael, J.A., Rea, A.H., Parrett, C., 2010. Predicting the probability and volume of postwildfire debris flows in the intermountain western United States. Geol. Soc. Am. Bull. 122 (1–2), 127–144. https://doi.org/10.1130/B26459.1.

Carabella, C., Miccadei, E., Paglia, G., Sciarra, N., 2019. Post-wildfire landslide hazard assessment: the case of the 2017 Montagna Del Morrone Fire (Central Apennines, Italy). Geosciences 9 (4), 175. https://doi.org/10.3390/geosciences9040175.

Cal Fire, 2022. Previous fire incidents by year. Retrieved from https://www.fire.ca.gov/incidents/2016/6/20/san-gabriel-complex-formerly-fish-reservoir-fires.

Chen, J., McGuire, K.J., Stewart, R.D., 2020. Effect of soil water-repellent layer depth on post-wildfire hydrological processes. Hydrol. Process. 34 (2), 270–283. https://doi.org/10.1002/hyp.13583.

Clark, J., Bobbe, T., Wulder, M., 2006. Using remote sensing to map and monitor fire damage in forest ecosystems. In: Wilder, M., Franklin, S. (Eds.), Forest Disturbance and Spatial Patterns, GIS and Remote Sensing Approaches, pp. 113–132.

Cleugh, H.A., Leuning, R., Mu, Q., Running, S.W., 2007. Regional evaporation estimates from flux tower and MODIS satellite data. Remote Sens. Environ. 106 (3), 285–304. https://doi.org/10.1016/j.rse.2006.07.007.
Conedera, M., Peter, L., Marxer, P., Forster, F., Rickenmann, D., Re, L., 2003. Consequences of forest fires on the hydrogeological response of mountain catchments: a case study of the Riale Buffaga, Ticino, Switzerland. Earth Surf. Process. Landf. 28 (2), 117–129. https://doi.org/10.1002/esp.425.
Daly, E., Porporato, A., 2006. Impact of hydroclimatic fluctuations on the soil water balance. Water Resour. Res. 42 (6) https://doi.org/10.1029/2005WR004606.
De Graff, J.V., 2014. Improvement in quantifying debris flow risk for post-wildfire emergency response. Geoenviron. Disasters 1 (1), 5. https://doi.org/10.1186/s40677-014-0005-2.
De Graff, J.V., 2018. A rationale for effective post-fire debris flow mitigation within forested terrain. Geoenviron. Disasters 5 (1), 7. https://doi.org/10.1186/s40677-018-0099-z.
Debano, L.F., 2000. The role of fire and soil heating on water repellency in wildland environments: a review. J. Hydrol. 231–232, 195–206. https://doi.org/10.1016/S0022-1694(00)00194-3.
Di Napoli, M., Marsiglia, P., Di Martire, D., Ramondini, M., Ullo, S.L., Calcaterra, D., 2020. Landslide susceptibility assessment of wildfire burnt areas through earth-observation techniques and a machine learning-based approach. Remote Sens. 12 (15), 2505. https://doi.org/10.3390/rs12152505.
DiBiase, R.A., Whipple, K.X., Heimsath, A.M., Ouimet, W.B., 2010. Landscape form and millennial erosion rates in the San Gabriel Mountains, CA. Earth Planet. Sci. Lett. 289 (1–2), 134–144. https://doi.org/10.1016/j.epsl.2009.10.036.
Doerr, S.H., Shakesby, R.A., Blake, W.H., Chafer, C.J., Humphreys, G.S., Wallbrink, P.J., 2006. Effects of differing wildfire severities on soil wettability and implications for hydrological response. J. Hydrol. 319 (1–4), 295–311. https://doi.org/10.1016/j.jhydrol.2005.06.038.
Donovan, I.P., Santi, P.M., 2017. A probabilistic approach to post-wildfire debris-flow volume modeling. Landslides 14 (4), 1345–1360. https://doi.org/10.1007/s10346-016-0786-3.
Ebel, B.A., Moody, J.A., 2020. Parameter estimation for multiple post-wildfire hydrologic models. Hydrol. Process. 34 (21), 4049–4066. https://doi.org/10.1002/hyp.13865.
Ebel, B.A., Wagenbrenner, J.W., Kinoshita, A.M., Bladon, K.D., 2022. Hydrologic recovery after wildfire: A framework of approaches, metrics, criteria, trajectories, and timescales. Journal of Hydrology and Hydromechanics 70 (4), 388–400. https://doi.org/10.2478/johh-2022-0033.
Farmer, D., Sivapalan, M., Jothityangkoon, C., 2003. Climate, soil, and vegetation controls upon the variability of water balance in temperate and semiarid landscapes: Downward approach to water balance analysis. Water Resour. Res. 39 (2) https://doi.org/10.1029/2001WR000328.
Fredlund, D.G., Rahardjo, H., 1993. Soil Mechanics for Unsaturated Soils. John Wiley & Sons.
Gardner, W.R., 1958. Some steady-state solutions of the unsaturated moisture flow equation with application to evaporation from a water table. Soil Sci. 85 (4).
Gartner, J.E., Cannon, S.H., Santi, P.M., Dewolfe, V.G., 2008. Empirical models to predict the volumes of debris flows generated by recently burned basins in the western U.S. Geomorphology 96 (3–4), 339–354. https://doi.org/10.1016/j.geomorph.2007.02.033.
Gehring, E., Conedera, M., Maringer, J., Giadrossich, F., Guastini, E., Schwarz, M., 2019. Shallow landslide disposition in burnt European beech (Fagus sylvatica L.) forests. Sci. Rep. 9 (1), 8638. https://doi.org/10.1038/s41598-019-45073-7.
Godt, J.W., Şener-Kaya, B., Lu, N., Baum, R.L., 2012. Stability of infinite slopes under transient partially saturated seepage conditions. Water Resour. Res. 48 (5) https://doi.org/10.1029/2011WR011408.
Gorsevski, P.V., Gessler, P.E., Boll, J., Elliot, W.J., Foltz, R.B., 2006. Spatially and temporally distributed modeling of landslide susceptibility. Geomorphology 80 (3–4), 178–198. https://doi.org/10.1016/j.geomorph.2006.02.011.
He, Y., Beighley, R.E., 2008. GIS-based regional landslide susceptibility mapping: a case study in southern California. Earth Surf. Process. Landf. 33 (3), 380–393. https://doi.org/10.1002/esp.1562.
Jackson, M., Roering, J.J., 2009. Post-fire geomorphic response in steep, forested landscapes: Oregon Coast Range, USA. Quat. Sci. Rev. 28 (11−12), 1131–1146. https://doi.org/10.1016/j.quascirev.2008.05.003.
Khalili, N., Habte, M.A., Zargarbashi, S., 2008. A fully coupled flow deformation model for cyclic analysis of unsaturated soils including hydraulic and mechanical hystereses. Comput. Geotech. 35 (6), 872–889. https://doi.org/10.1016/j.compgeo.2008.08.003.
Kozak, J.A., Ahuja, L.R., Green, T.R., Ma, L., 2007. Modelling crop canopy and residue rainfall interception effects on soil hydrological components for semi-arid agriculture. Hydrol. Process. 21 (2), 229–241. https://doi.org/10.1002/hyp.6235.
Lei, M., Cui, Y., Ni, J., Zhang, G., Li, Y., Wang, H., et al., 2022. Temporal evolution of the hydromechanical properties of soil-root systems in a forest fire in China. Sci. Total Environ. 809, 151165 https://doi.org/10.1016/j.scitotenv.2021.151165.
Los, S.O., Pollack, N.H., Parris, M.T., Collatz, G.J., Tucker, C.J., Sellers, P.J., et al., 2000. A global 9-yr biophysical land surface dataset from NOAA AVHRR data. J. Hydrometeorol. 1 (2), 183–199. https://doi.org/10.1175/1525-7541(2000)001<0183:AGYBLS>2.0.CO;2.
Madadgar, S., Sadegh, M., Chiang, F., Ragno, E., AghaKouchak, A., 2020. Quantifying increased fire risk in California in response to different levels of warming and drying. Stoch. Env. Res. Risk A. 34 (12), 2023–2031. https://doi.org/10.1007/s00477-020-01885-y.
Masi, E.B., Segoni, S., Tofani, V., 2021. Root reinforcement in slope stability models: a review. Geosciences 11 (5), 212. https://doi.org/10.3390/geosciences11050212.
May, C.L., Gresswell, R.E., 2004. Spatial and temporal patterns of debris-flow deposition in the Oregon Coast Range, USA. Geomorphology 57 (3–4), 135–149. https://doi.org/10.1016/S0169-555X(03)00086-2.
McGuire, L.A., Rengers, F.K., Kean, J.W., Staley, D.M., Tang, H., Youberg, A.M., 2019. Looking through the Window of Disturbance at Post-Wildfire Debris Flow Hazards. Colorado School of Mines. Arthur Lakes Library.
Melo, R., Zêzere, J.L., 2017. Modeling debris flow initiation and run-out in recently burned areas using data-driven methods. Nat. Hazards 88 (3), 1373–1407. https://doi.org/10.1007/s11069-017-2921-4.
Meng, R., Dennison, P.E., D'Antonio, C.M., Moritz, M.A., 2014. Remote sensing analysis of vegetation recovery following short-interval fires in Southern California Shrublands. PLoS One 9 (10), e110637. https://doi.org/10.1371/journal.pone.0110637.
Merriam, R.A., 1960. A note on the interception loss equation. J. Geophys. Res. 65 (11), 3850–3851. https://doi.org/10.1029/JZ065i011p03850.
Milledge, D.G., Griffiths, D.V., Lane, S.N., Warburton, J., 2012. Limits on the validity of infinite length assumptions for modelling shallow landslides. Earth Surface Processes and Landforms 37 (11), 1158–1166.
Monteith, J.L., 1965. Evaporation and environment. In: Symposia of the Society for Experimental Biology, vol. 19. Cambridge University Press (CUP), Cambridge, pp. 205–234.
Moody, J.A., Shakesby, R.A., Robichaud, P.R., Cannon, S.H., Martin, D.A., 2013. Current research issues related to post-wildfire runoff and erosion processes. Earth Sci. Rev. 122, 10–37. https://doi.org/10.1016/j.earscirev.2013.03.004.
Mu, Q., Heinsch, F.A., Zhao, M., Running, S.W., 2007. Development of a global evapotranspiration algorithm based on MODIS and global meteorology data. Remote Sens. Environ. 111 (4), 519–536. https://doi.org/10.1016/j.rse.2007.04.015.
Mu, Q., Zhao, M., Running, S.W., 2011. Improvements to a MODIS global terrestrial evapotranspiration algorithm. Remote Sens. Environ. 115 (8), 1781–1800. https://doi.org/10.1016/j.rse.2011.02.019.
Nyman, P., Sheridan, G.J., Smith, H.G., Lane, P.N.J., 2011. Evidence of debris flow occurrence after wildfire in upland catchments of south-East Australia. Geomorphology 125 (3), 383–401. https://doi.org/10.1016/j.geomorph.2010.10.016.
NCEI, 2023. NCEI's Climate Data Online Page. Retrieved from https://www.ncei.noaa.gov/cdo-web/datasets/GHCND/stations/GHCND:USC00047779/detail.
NIFC, 2022. National Interagency Fire Center, Statistics, Retrieved from https://www.nifc.gov/fire-information/statistics.
Parise, M., Cannon, S.H., 2012. Wildfire impacts on the processes that generate debris flows in burned watersheds. Nat. Hazards 61 (1), 217–227. https://doi.org/10.1007/s11069-011-9769-9.
Peduto, D., Iervolino, L., Esposito, G., Foresta, V., Matano, F., Masi, R., 2022. Clues of wildfire-induced geotechnical changes in volcanic soils affected by post-fire slope instabilities. Bulletin of Engineering Geology and the Environment 81 (10), 454. https://doi.org/10.1007/s10064-022-02947-x.
Parsons, A., Robichaud, P.R., Lewis, S.A., Napper, C. & Clark, J.T., 2010. Field Guide for Mapping Post-Fire Soil Burn Severity. https://www.fs.fed.us/rm/pubs/rmrs_gtr243.pdf.
Ragno, E., AghaKouchak, A., Love, C.A., Cheng, L., Vahedifard, F., Lima, C.H.R., 2018. Quantifying changes in future intensity-duration-frequency curves using multimodel ensemble simulations. Water Resour. Res. 54 (3), 1751–1764. https://doi.org/10.1002/2017WR021975.
Raymond, C.A., McGuire, L.A., Youberg, A.M., Staley, D.M., Kean, J.W., 2020. Thresholds for post-wildfire debris flows: insights from the Pinal Fire, Arizona, USA. Earth Surf. Process. Landf. 45 (6), 1349–1360. https://doi.org/10.1002/esp.4805.
Rengers, F.K., 2020. Inventory of landslides triggered by rainfall on 16-17 January 2019, Los Angeles County, CA. https://doi.org/10.5066/P97GU3UV.
Rengers, F.K., McGuire, L.A., Kean, J.W., Staley, D.M., Hobley, D.E.J., 2016. Model simulations of flood and debris flow timing in steep catchments after wildfire. Water Resour. Res. 52 (8), 6041–6061. https://doi.org/10.1002/2015WR018176.
Rengers, Francis K., McGuire, L.A., Oakley, N.S., Kean, J.W., Staley, D.M., Tang, H., 2020. Landslides after wildfire: initiation, magnitude, and mobility. Landslides 17 (11), 2631–2641. https://doi.org/10.1007/s10346-020-01506-3.
Richards, L.A., 1931. Capillary conduction of liquids through porous mediums. Physics 1 (5), 318–333. https://doi.org/10.1063/1.1745010.
Robichaud, P.R., 2000. Evaluating the Effectiveness of Postfire Rehabilitation Treatments. US Department of Agriculture, Forest Service, Rocky Mountain Research Station.
Rulli, M.C., Rosso, R., 2005. Modeling catchment erosion after wildfires in the San Gabriel Mountains of southern California. Geophys. Res. Lett. 32 (19) https://doi.org/10.1029/2005GL023635 n/a-n/a.
Schaap, M.G., Leij, F.J., van Genuchten, M.Th., 2001. Rosetta : a computer program for estimating soil hydraulic parameters with hierarchical pedotransfer functions. J. Hydrol. 251 (3–4), 163–176. https://doi.org/10.1016/S0022-1694(01)00466-8.
Schmidt, K.M., Roering, J.J., Stock, J.D., Dietrich, W.E., Montgomery, D.R., Schaub, T., 2001. The variability of root cohesion as an influence on shallow landslide susceptibility in the Oregon Coast Range. Canadian Geotechnical Journal 38 (5), 995–1024. https://doi.org/10.1139/cgj-38-5-995.
Shakesby, R.A., Doerr, S.H., 2006. Wildfire as a hydrological and geomorphological agent. Earth Sci. Rev. 74 (3–4), 269–307. https://doi.org/10.1016/J.EARSCIREV.2005.10.006.
Sidle, R.C., 1991. A conceptual model of changes in root cohesion in response to vegetation management. J. Environ. Qual. 20 (1), 43–52. https://doi.org/10.2134/jeq1991.00472425002000010009x.
Staley, D.M., Negri, J.A., Kean, J.W., Laber, J.L., Tillery, A.C., Youberg, A.M., 2017. Prediction of spatially explicit rainfall intensity–duration thresholds for post-fire

debris-flow generation in the western United States. Geomorphology 278, 149–162. https://doi.org/10.1016/j.geomorph.2016.10.019.
Sternberg, P.D., Anderson, M.A., Graham, R.C., Beyers, J.L., Tice, K.R., 1996. Root distribution and seasonal water status in weathered granitic bedrock under chaparral. Geoderma 72 (1–2), 89–98. https://doi.org/10.1016/0016-7061(96)00019-5.
Stoof, C.R., Vervoort, R.W., Iwema, J., van den Elsen, E., Ferreira, A.J.D., Ritsema, C.J., 2012. Hydrological response of a small catchment burned by experimental fire. Hydrol. Earth Syst. Sci. 16 (2), 267–285. https://doi.org/10.5194/hess-16-267-2012.
Tang, H., McGuire, L.A., Rengers, F.K., Kean, J.W., Staley, D.M., Smith, J.B., 2019. Evolution of debris-flow initiation mechanisms and sediment sources during a sequence of postwildfire rainstorms. J. Geophys. Res. Earth 124 (6), 1572–1595. https://doi.org/10.1029/2018JF004837.
Taylor, D.W., 1948. Fundamentals of Soil Mechanics. Soil Sci. 66 (2).
Terwilliger, V.J., 1988. Mechanical Effects of Chaparral Disturbances on Soil Slip Patterns in the Transverse Ranges of Southern California. University of California, Los Angeles.
Terwilliger, V.J., Waldron, L.J., 1991. Effects of root reinforcement on soil-slip patterns in the Transverse Ranges of southern California. Geol. Soc. Am. Bull. 103 (6), 775–785. https://doi.org/10.1130/0016-7606(1991)103<0775:EORROS>2.3.CO;2.
Thomas, H.R., He, Y., 1997. A coupled heat-moisture transfer theory for deformable unsaturated soil and its algorithmic implementation. Int. J. Numer. Methods Eng. 40 (18), 3421–3441. https://doi.org/10.1002/(SICI)1097-0207(19970930)40:18<3421::AID-NME220>3.0.CO;2-C.
Thomas, M.A., Rengers, F.K., Kean, J.W., McGuire, L.A., Staley, D.M., Barnhart, K.R., Ebel, B.A., 2021. Post wildfire soil-hydraulic recovery and the persistence of debris flow hazards. J. Geophys. Res. Earth 126 (6). https://doi.org/10.1029/2021JF006091.
Tracy, F.T., Vahedifard, F., 2022. Analytical solution for coupled hydro-mechanical modeling of infiltration in unsaturated soils. J. Hydrol. 612, 128198 https://doi.org/10.1016/j.jhydrol.2022.128198.
Tracy, F.T., Vahedifard, F., 2023. Two-dimensional analytical solution for transient flow in unsaturated soils considering hydromechanical coupling. Water Resour. Res. 59 (12) e2023WR035326.
Vahedifard, F., Abdollahi, M., Leshchinsky, B.A., Stark, T.D., Sadegh, M., AghaKouchak, A., 2024. Interdependencies between wildfire-induced alterations in soil properties, near-surface processes, and geohazards. Earth Space Sci. 11 (2) e2023EA003498.
Varela, M.E., Benito, E., Keizer, J.J., 2015. Influence of wildfire severity on soil physical degradation in two pine forest stands of NW Spain. CATENA 133, 342–348. https://doi.org/10.1016/j.catena.2015.06.004.
Vergani, C., Werlen, M., Conedera, M., Cohen, D., Schwarz, M., 2017. Investigation of root reinforcement decay after a forest fire in a Scots pine (Pinus sylvestris) protection forest. For. Ecol. Manag. 400, 339–352. https://doi.org/10.1016/j.foreco.2017.06.005.
von Hoyningen-Huene, J., 1981. Die Interzeption des Niederschlags in landwirtschaftlichen Pflanzenbeständen. Arbeitsbericht Deutscher Verband für Wasserwirtschaft und Kulturbau, DVWK.
Wagenbrenner, J.W., Ebel, B.A., Bladon, K.D., Kinoshita, A.M., 2021. Post-wildfire hydrologic recovery in Mediterranean climates: A systematic review and case study to identify current knowledge and opportunities. Journal of Hydrology 602, 126772. https://doi.org/10.1016/j.jhydrol.2021.126772.
Williams, A.P., Abatzoglou, J.T., Gershunov, A., Guzman-Morales, J., Bishop, D.A., Balch, J.K., Lettenmaier, D.P., 2019. Observed impacts of anthropogenic climate change on wildfire in California. Earth's Future 7 (8), 892–910. https://doi.org/10.1029/2019EF001210.
Wohlgemuth, P.M., Hubbert, K.R., 2008. The effects of fire on soil hydrologic properties and sediment fluxes in chaparral steeplands, southern California. In: Narog, Marcia G., tech. coord (Eds.), Proceedings of the 2002 Fire Conference: Managing Fire and Fuels in the Remaining Wildlands and Open Spaces of the Southwestern United States. Gen. Tech. Rep. PSW-GTR-189, vol. 189. US Department of Agriculture, Albany, CA, pp. 115–122.
Wu, T.H., McKinnell, Swanston, D.N., 1979. Strength of tree roots and landslides on Prince of Wales Island, Alaska. Canadian Geotechnical Journal 16 (1), 19–33. https://doi.org/10.1139/t79-003.
Wu, L.Z., Zhang, L.M., 2009. Analytical solution to 1D coupled water infiltration and deformation in unsaturated soils. Int. J. Numer. Anal. Methods Geomech. 33 (6), 773–790. https://doi.org/10.1002/nag.742.
Zhang, L.L., Fredlund, D.G., Fredlund, M.D., Wilson, G.W., 2014. Modeling the unsaturated soil zone in slope stability analysis. Can. Geotech. J. 51 (12), 1384–1398. https://doi.org/10.1139/cgj-2013-0394.
Zhuang, Y., Xing, A.G., Jiang, Y.H., Sun, Q., Yan, J.K., Zhang, Y.B., 2022. Typhoon, rainfall and trees jointly cause landslides in coastal regions. Eng Geol 298.